

Hyperspectral Remote Sensing Imagery Generation From RGB Images Based on Joint Discrimination

Liqin Liu, Sen Lei, Zhenwei Shi*, Member, IEEE, Ning Zhang, Xinzong Zhu

Abstract—Spatial resolution and spectral resolution both play an important role in the recognition of objects in hyperspectral remote sensing. However, the imaging characteristics of hyperspectral images (HSI) result in a mutually restrictive relationship between the spatial and spectral resolutions. Generative adversarial networks (GAN) have achieved significant success in image generation. The introduction of the discriminators plays a key role in improving the reality. In this paper, we propose an RGB To multi-band Hyperspectral imagery (150 bands) generation method based on GAN (R2HGAN). The method solves the high ill-posed problem and introduces high spectral resolution into RGB images by learning from multiple scenes of HSI. In R2HGAN, we extend the adversarial learning from spatial to spectral dimensions and joint discrimination is designed to generate HSIs closer to the real ones, where two discriminators (the conditional D and the spectral D) are put forward to supervise the spectral similarity and the conditional reality of the HSI jointly. In detail, the conditional discriminator comprehensively judges the quality of each area in the reconstructed HSI. At the same time, to ensure that the generated spectra are close to the real ones, a spectral discriminator based on Multilayer Perceptron (MLP) is designed. Through the experiments on GF-5 imagery, the method has significantly improved the quality of the generated images over other state-of-the-art methods.

Index Terms—Hyperspectral image, remote sensing, Generation Adversarial Network (GAN), spectral super-resolution (SSR)

I. INTRODUCTION

THE hyperspectral image (HSI) is a 3D-cube, which contains spatial and spectral information at the same time. Compared with RGB and multi-spectral remote sensing images (MSI), HSIs' high spectral resolution is of great significance for identifying the diagnostic spectrum of ground objects. Therefore, HSIs have been widely applied on precision agriculture [1], ecological sciences [2], mineralogy [3] and other fields. In the past 30 years, HSI processing technology has made great progress, including HSI classification [4–7], target detection [8, 9], anomaly detection [10], hyperspectral unmixing [11–13] and so on [14]. Among the above

The work was supported by the National Key RD Program of China under the Grant 2019YFC1510905, the National Natural Science Foundation of China under the Grant 61671037, the Beijing Natural Science Foundation under the Grant 4192034 and Shanghai Association for Science and Technology under the Grant SAST2020077. (Corresponding author: Zhenwei Shi (e-mail: shizhenwei@buaa.edu.cn))

Liqin Liu, Sen Lei and Zhenwei Shi are with Image Processing Center, School of Astronautics, Beihang University, Beijing 100191, China, and with Beijing Key Laboratory of Digital Media, Beihang University, Beijing 100191, China, and also with State Key Laboratory of Virtual Reality Technology and Systems, School of Astronautics, Beihang University, Beijing 100191, China.

Ning Zhang and Xinzong Zhu are with Shanghai Aerospace Electronic Technology Institute, Shanghai 201109, China.

techniques, spatial information is widely used and plays an important role. Therefore, we hope to get imagery with both high spatial and spectral resolutions.

In remote sensing imaging, the spectral and spatial resolutions restrict each other under the same imaging time due to the architectural constraints of the imaging system [15]. Many RGB or MSI images with high spatial resolution usually lack spectral information. For example, Chinese Gaofen-1 (GF-1) with spatial resolution of 8m/pixel has 4 bands covering wavelength $0.45 - 0.89\mu m$ [16] and Gaofen-2 provides 4 band MSI with spatial resolution of 4m/pixel. Landsat 8 has 7 bands with spatial resolution of 30m/pixel covering the wavelength range of $0.433 - 2.3\mu m$ [17]. Besides, hyperspectral imagery mainly with a low spatial resolution. For satellite HSI, the spatial resolution is even lower than 20m/pixel, such as the resolution of Chinese GaoFen-5 (GF5) [18] and Earth observation (EO)-1 Hyperion [19] are both 30m/pixel. At present, it is difficult to obtain remote sensing images with high spatial and spectral resolution at the same time.

Since the spatial resolution and the spectral resolution are very important for hyperspectral images, and the imaging equipment limits the simultaneous acquisition of good spatial and spectral resolutions, some post-acquisition methods are widely used [19, 20]. That is, through enhancement techniques to improve the spatial resolution [20] of HSI or to increase the spectral resolution of images with a higher spatial resolution [19] (such as RGB and MSI).

A typical way to improve the spatial resolution of HSI is hyperspectral super-resolution (HSI SR) [20, 21]. The SR methods can be classified into two representative categories, one is SR only use the low-resolution HSI (LR-HSI) [22, 23], another contains the methods that enhance the spatial resolution of HSI with the spatial information in high-resolution RGB or multispectral images (MSI) [24, 25]. The HSI SR can improve the spatial resolution on the basis of existing HSI.

Unlike HSI super-resolution, spectral super-resolution (SSR) promotes the spectral resolution of the image, which has attracted significant attention in recent years. SSR can provide high spatial resolution HSI only from a multispectral or RGB image without the use of hyperspectral sensors, which saves a lot of imaging hardware. Some SSR methods are designed to increase the channels of the multi-spectral image [26, 27]. Besides, a typical SSR application is spectral reconstruction from RGB images [28, 29].

The SSR methods from RGB images can provide HSI only with the RGB input, which makes SSR unique advantages in acquiring hyperspectral images with high spatial and spectral resolution at the same time. However, there are two main short-

comings of the existing remote sensing HSI reconstruction methods:

- 1) The methods are usually training and testing on a single scene, lacking a large amount of data support, and cannot reflect the universal mapping between RGB and spectrum of different ground objects. Besides, they usually recover HSI from more than 4 bands. For example, Mei *et al.* recover HSI from 4 or 6 bands [26] use the 3D-CNN on PaviaU or Cuprite dataset which only in one scene. In [27], several standard benchmark datasets which are single scene images or their subsets are adopted.
- 2) Most methods use CNN and other structures to constrain the pixel-wise distance between the generated image and the real image, MSE or \mathcal{L}_1 loss is usually adopted. Mei *et al.* adopt \mathcal{L}_1 loss to train networks [26]. Arun *et al.* use multi-loss functions including MSE loss and SAM loss [27]. In [30], Gewali *et al.* use 1D-CNN for single-pixel SSR and propose a new spectral loss function to constrain the Euclidean distances and first, second derivatives between the generated HSI and the real one. It is easy to cause over-smoothing or even some generation that does not meet the actual situation. The framework affects diversity and reality of the spectra.

To overcome these problems, we propose a Generative Adversarial Networks (GAN)-based framework to generate HSI from RGB. The model can export 150 bands HSI with RGB input without the need for any HSI. It is trained on multiple scenes GF-5 HSI, thus it provides the non-linear mapping of RGB to spectrum. In addition to the traditional minimize pixel-wise error and keep fitting, a GAN-based framework and joint discrimination by two discriminators are devised. One is the conditional discriminator based on PatchGAN [31] to distinguish whether true or false of multiple regions in the HSI. Another is spectral discriminator based on MLP to determine whether the spectra sampled from HSI is true. Meanwhile, the Random Global Uniform Sampling (RGUS) technique is applied for sampling a limited number of spectra from HSI as the overall expression of it. The experimental results show that R2HGAN outperforms other state-of-the-art methods on various indicators. Codes of R2HGAN are available at <http://levir.buaa.edu.cn/Code.htm>.

In summary, the main contributions can be summarized as follows.

- 1) We provide a general framework for RGB to HSI (R2HGAN) and experiment it on multiple scenes. The framework reveals the general mapping between RGB values of each pixel and its corresponding spectrum in large amounts of data. Meanwhile, it is based on GAN to avoid overfitting and abnormal generation.
- 2) We extend the adversarial learning from spatial to spectral dimensions. In addition to the traditional existing conditional discriminator, we design a spectral discriminator based on MLP together with the conditional discriminator to generate HSIs closer to the real ones by joint discrimination. Two discriminators separately supervise the conditional and spectral reality of the generated HSI, and the generator can export more realistic HSI on spectral

and spatial.

The paper is organized as follows. Section 2 introduces the related works on HSI reconstruction and GAN, Section 3 details the proposed method. Section 4 provides experimental evaluations of the proposed method on the dataset and Section 5 concludes the paper.

II. RELATED WORK

In this section, we introduce the two hyperspectral image reconstruction methods including HSI Super-Resolution (SR) and Spectral Super-resolution (SSR) from RGB images. Meanwhile, a brief introduction of GAN and its use on image generation, remote sensing image processing is exhibited. Various indicators used for evaluating on the quality of reconstruction is demonstrated at last.

A. Hyperspectral Image Super-Resolution

The HSI SR mainly includes two types of methods: super-resolution from low-resolution HSI (LR-HSI) only and fusion of high spatial resolution RGB/MSI and low spatial resolution HSI.

Akgun *et al.* represent different wavelengths as weighted linear combinations of a small number of aliased and blurred basis image planes and solve the SR problem by a set-theoretic method [20]. Similarly, many researches use the inter-band information for SR [22, 32]. In [32], Hu *et al.* use very deep CNN (VDSR) for key-bands, SDCNN for other bands, and spatial-error-correction (SEC) model to correct the spatial error. Intrafusion Network [22] utilizes spatial-spectral information and reconstructs high-resolution HSI (HR-HSI) directly. Hu *et al.* propose a 3D-CNN-based method that integrates multiscale features for SR. Many GAN-based methods introduce the discriminator to judge the reality of HR-HSI [23]. Li *et al.* adopt band attention to promote the consistency of generated spectra [23]. In addition, Bayes based single image super-resolution method proposed by [33] transforms the problem of ill-posed SR reconstruction in the frequency domain into a quadratic optimization problem of abundance mapping and solves it by energy minimization (EM) method based on MRF. These methods require LR-HSI without need of corresponding MSI/RGB images.

In addition to the previous means, more HSI SR methods use other images with high spatial resolution and make full use of the spatial information [34, 35]. On this basis, some research base on the sparsity of HSI [21, 24, 35–38] to reconstruct the HR-HSI; some authors study on the self-similarity between local and nonlocal patches [25, 34–36] and the low rank of them [38–40]; some literatures have use or model the imaging principles and degradation process for super-resolution [24, 41, 42]. From the perspective of the solution process: dictionary-based methods are common such as [25, 38, 39]. Since HSI is a 3D-tensor, Xu *et al.* provide a *t*-product [35] to establish the relationship between HR-HSI and LR-HSI and constraint nonlocal similarity, Li *et al.* [37] propose a fusion method based on Coupled Sparse Tensor Decomposition (CSTF), Dian *et al.* compose 4D-Tensor with similar HSI patches [40], and transform HSI SR problem into

LTTR regularization constraint by using low-rank property. In [41, 42], CNN is used to fit the reconstruction process, and in [41] GAN [43] is adopted for SR. Kwon and Tai [21] guide the up-sampling process of LR-HSI by RGB and spectrum substitution to refine the upsampled spectra. Borsoi *et al.* [44] adopt spectral unmixing and model the spectral variability to study the SR problem of seasonal variation. The fusion methods of HSI and MSI (or RGB) make use of spatial information to achieve more accurate super-resolution. Compared with HSI only methods, they need to correspond other images in the scene, which is difficult to obtain in many cases.

The two kinds of HSI HR methods all need HSI with low resolution, which still need hyperspectral sensors. Usually, the cost of hyperspectral sensors is expensive due to complicated optics and electronics [45]. Therefore, many times the acquisition of LR-HSI is hard to satisfy.

B. Spectral Super-resolution

Different from HSI SR needs HSI input, the spectral super-resolution (SSR) reduces requirements on the spectral resolution of input images. SSR restores HSI with the high spatial resolution images, such as multi-spectral images (MSI) or RGB images.

To our knowledge, SSR methods for remote sensing mainly recover HSI from MSI and most methods work on one scene which lack applicability. For example, Mei *et al.* use 3D-CNN for simultaneous spatial and spectral super-resolution [26] and experiment on datasets for classification to select a patch for testing while others for training. Besides, many CNN based methods are adopted [27, 30]. In [30], a 1D-CNN is designed with tunable spectral sub-sampling layer and in loss function not only the Euclidean distances are constrained but also the first and second derivatives. [15, 19, 46] enhance spectral resolution by dictionary learning and spectral sparse. In [15], the authors adopt coupled dictionary learning along with sparse representations based on the assumption that the sparse codes in MSI and HSI are the same. Yi *et al.* use both the spectral improvement and the spatial preservation strategies to enhance the spectral information while retaining the spatial one for HSI reconstruction [19]. Meanwhile, Arun *et al.* and Sun *et al.* extract endmembers from MSI and reconstruct HSI from the abundance map [27, 47]. Arun *et al.* combines the collaborative unmixing process and correct the pixel-level reconstruction results [27], where 3D-CNN is used to combine spatial information.

Comparing to MSI, RGB imaging is simpler and requires less hardware. Many methods generate HSI from RGB images in natural scene. Some methods use image priors such as Yan *et al.* introduce category and location information into the network [48]. In [49], the authors adopt dictionary learning and in [50] manifold learning is used for the HSI generating. The most common RGB to HSI reconstruction methods are based on CNN [51, 52]. Pixel and channel attention are adopted in methods [53, 54] to expand the receptive field or focus on key channels. Li *et al.* provide 3D-RAN to extract contextual information between bands [53] and attention is

adopted to weight different channels. Zhao *et al.* propose a four-layer hierarchical regression network [54] and increase the receptive field by establishing an attention mechanism for the residual global module. In [28, 55], the authors take the imaging mechanism and physically plausible into account to constrain the SSR process. Nie *et al.* [55] learn spectral response functions (SRF) using modern filmfilter techniques. Shi *et al.* [56] upsample the bands and learn residuals to achieve accurate spectral recovery. Several methods [57, 58] use a GAN discriminator to ensure the reality of generated HSI. These methods are all based on natural HSI data such as ICVL [49, 50], Bgu HS [51, 53], and Arad HS [54, 59]. They mainly generate 31 bands from RGB images, which different from the remote sensing HSI generating to 150 bands.

We can find that there lacks SSR technology for reconstructing multi-band remote sensing HSI from RGB images.

C. GAN on generation and remote sensing image processing

Generative Adversarial Network (GAN) was proposed in 2014 [43] and has been widely used in various fields such as image generation [31, 60], image style transform [61, 62], and image super-resolution [63, 64]. GAN is composed of a generator G and a discriminator D , the G and D zero-sum game, jointly promote each other.

Image generation is to generate specific images from other images or text. The HSI reconstruction can be seen as a generation from RGB to HSI. GAN has been widely used on image generation. A generator aims to generate a target image from an image or other input and the discriminator aims to distinguish whether the image generated is real or not. Early methods used GAN [43] and its improvements to generate [65, 66]. After that, a number of hierarchical generation methods are used to generate an image closer and closer to the target one, such as StackGAN [67], LAPGAN [68] and PGGAN [69]. In [31], a generic image-to-image translation framework based on CGAN [70] is proposed and PatchGAN is proposed to improve the discriminator on output. Different from the pair image generation or style transform, unsupervised generation methods have also been gradually developed. CycleGAN [62] use cycle-consistent to realize unpair image translation. Meanwhile, DualGAN [71] and DiscoGAN [72] adopt a similar approach. In addition to one-to-one generation, many one-to-many generation methods have been developed, most of which are implemented by introducing latent code [73, 74]. A typical method is StyleGAN [61, 75], it aims to generating image with a specific style or obtaining corresponding style image from latent code.

GAN has also achieved ideal results on remote sensing image processing [64, 76]. [77] is a GAN model for unsupervised pan-sharpening. Zhao *et al.* study on remote sensing change detection via GAN [78]. In [64, 76], the authors use GAN for remote sensing super-resolution. GAN is also used for cloud detection [79] and scene classification [80]. Many studies use GAN for hyperspectral anomaly detection [10], classification [81] while Mehta *et al.* adopt GAN for HSI dehazing [82].

In this paper, we will adopt GAN for the reconstruction of HSI from RGB images.

D. Quantitative Metrics on HSI reconstruction

At present, the evaluation indicators used in the literature that recover HSI from RGB are different, and we will introduce the commonly used ones below. Let $I_R^{(i)}$ represents the i th spectrum in the real HSI and $I_G^{(i)}$ the i th spectrum in the generated HSI. n is the total number of spectra. d represents the number of bands in HSI.

- **RMSE (Root Mean Squared Error)** measures the pixel-wise square root error between spectra generated and the real. It is the most commonly used metric in RGB-to-HSI research [19, 28, 30, 48, 49, 51–58].

$$RMSE = \sqrt{\frac{1}{n} \sum_{i=1}^n (I_R^{(i)} - I_G^{(i)})^2} \quad (1)$$

- **MRAE (Mean Relative Absolute Error)** is the magnitude of the error relative to the true value. Same as RMSE, they both measure the distance between the spectrum and its true value, except that MRAE is the error related to the L_1 norm [28, 48, 52–54, 56, 58].

$$MRAE = \frac{1}{n} \sum_{i=1}^n \frac{|I_R^{(i)} - I_G^{(i)}|}{I_G^{(i)}} \quad (2)$$

- **MPSNR (Mean Peak Signal-to-Noise Ratio)**. PSNR is often used as a measurement of signal reconstruction quality in image compression and other fields, and it can be derived from MSE (Mean Squared Error). For HSI, we need to calculate PSNR for different bands separately, and then take the average value, which is called MPSNR [19, 26, 27, 53]. Similar to MRAE, MPSNR reflects the relative magnitude between the error and real HSI.

$$\begin{aligned} MSE_j &= \frac{1}{n} \sum_{i=1}^n (I_R^{(i,j)} - I_G^{(i,j)})^2 \\ MPSNR &= \frac{1}{d} \sum_{j=1}^d 10 \times \lg\left(\frac{MAX_j}{MSE_j}\right) \end{aligned} \quad (3)$$

In Eq.(3), MSE_j is the MSE of j th band and MAX_j is the max possible value in j th band of real HSI. $I_{R/G}^{(i,j)}$ is the j th intensity in i th spectrum.

- **SAM (Spectral Angle Mapper)** reflects the spectral angular distance between the generated spectrum and the real one. Different from MPSNR or MRAE, SAM has more constraints on the shape of the generated spectrum [19, 26, 27, 30, 47, 48, 51–53].

$$SAM = \frac{1}{n} \sum_{i=1}^n \cos^{-1} \frac{I_R^{(i)} T I_G^{(i)}}{(I_R^{(i)} T I_R^{(i)})^{1/2} (I_G^{(i)} T I_G^{(i)})^{1/2}} \quad (4)$$

- **MSSIM (Mean Structural SIMmilarity)**. SSIM is a measurement proposed in [83]. Unlike RMSE and MRAE which measure error visibility, SSIM measures the structural similarity of two bands. MSSIM is the mean of SSIM of every generated HSI band and the real [19, 26, 27, 53].

$$MSSIM = \frac{1}{d} \sum_{j=1}^d \frac{(2\mu_R^j \mu_G^j + C_1)(2\sigma_{RG}^{jj} + C_2)}{(\mu_R^j)^2 + (\mu_G^j)^2 + C_1(\sigma_R^j)^2 + \sigma_G^j)^2 + C_2} \quad (5)$$

Where $\mu_{G/R}^j$ and $\sigma_{G/R}^j$ denote the mean and standard of patch in j th band of generated or real HSI. σ_{RG}^{jj} is the covariance between the patches in j th band in R and j th band in G. $C_1 = (K_1 \times L)^2$ and $C_2 = (K_2 \times L)^2$ are constants where L denotes the dynamic range of pixel values and we select $K_1 = 0.01$, $K_2 = 0.03$, $L = 65535$.

In addition, there are also other indicators adopted, such as NRMSE [50], ERGAS [47] and SSM [27] which evaluate pixel-wise error; GFC [58], CC [19] and R [30] from the perspective of relevance; ΔE [58], BPMRAE [54] that is colormetric based.

In this paper, we will compare R2HGAN with other state-of-the-art methods on RMSE, MRAE, SAM, MSSIM and MPRNR to comprehensively evaluate the recovery result.

III. PROPOSED METHOD

In this paper, we propose a 3 to 150 bands mapping framework for HSI reconstruction and experiment it on multiple scene images. To promote the diversity and the reality of the generated HSI, we design a joint discrimination method under the GAN framework. One discriminator is designed as a conditional PatchGAN which supervises the consistency between HSI and input RGB. It outputs a patch in which each element represents the performance of a region in HSI. Another discriminator is proposed to ensure the physical reality of the generated spectra. Meanwhile, Random Global Uniform Sampling (RGUS) technique samples the spectra in HSI, and then they are input to the MLP to get reality scores for every one. The flowchart of R2HGAN is illustrated in Fig. 1.

A. U-Net Generator

To make use of multi-scale features of RGB image and generate an HSI containing semantic characteristics and detailed information in both, we design a U-Net for the Generator (G). In G encoder, to realize rapid reduction of the image size, there are 8 Conv-layers with $kernel_size = 4 \times 4$, $stride = 2$ each followed by Leaky ReLU. To save computing resources, we adopt convolutional kernel with $kernel_size = 4 \times 4$, $stride = 2$ instead of $kernel_size = 44$, $stride = 1$ and 2×2 pooling. In the encoder, the size of feature maps is down by half layer by layer. Since the input image size is cropped to 256×256 , to leverage information at the deepest semantic level, 8 conv-layer are used one by one. After 8 downsampling, the size becomes $1/2^8 = 1/256$ of the input image. We utilize deconv $kernel_size = 4 \times 4$, $stride = 2$ for upsample and before it, ReLU is used for activation. In the first three layers in the decoder, dropout with $keep_prob = 0.5$ is adopted to avoid overfitting. After the concatenate with 7 encoder layers, a deconv layer followed by Tanh activation restores the 150-channel HSI. It is worth noting that we removed all the BN layers in G as we select $batchsize = 1$ for the generator because it is well known that BN will cause poor effect when batch size is small [51].

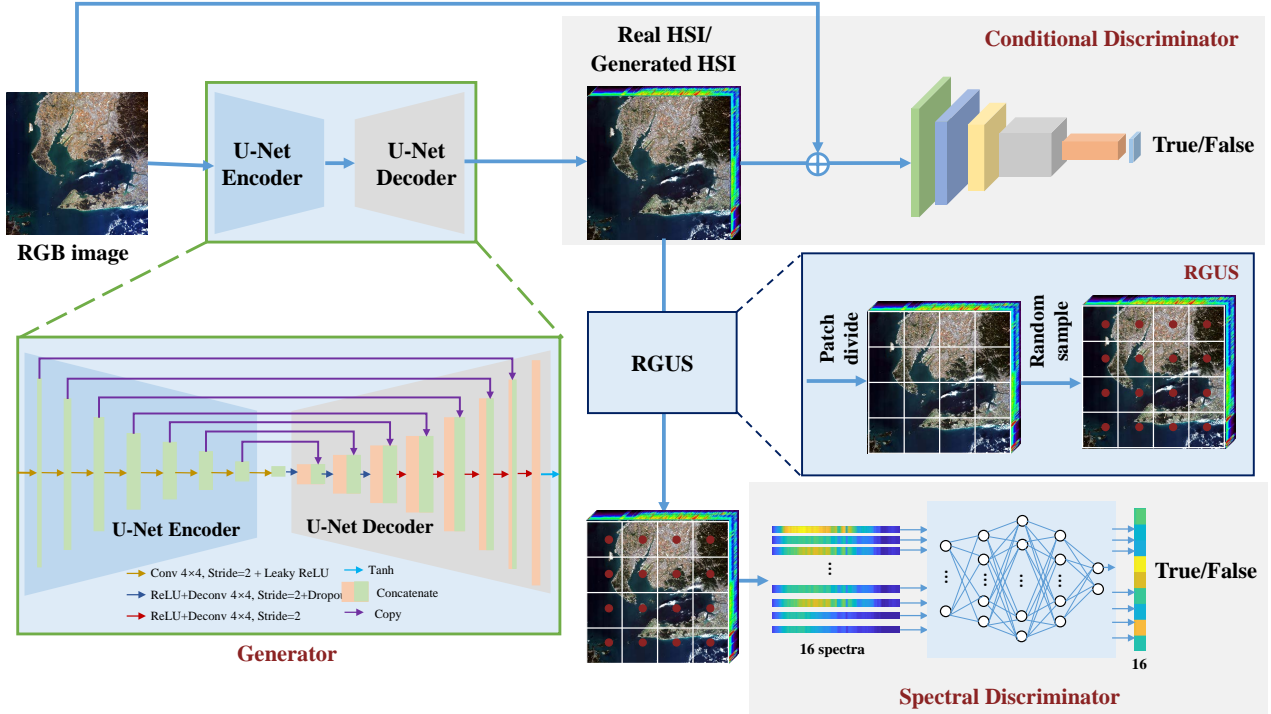


Fig. 1. The flowchart of R2HGAN. We design a U-Net generator to fully integrate features of different semantic levels thus get a more precise HSI. The Generator consists of an 8-layer convolutional encoder and a corresponding decoder. Joint discrimination is conducted by conditional discriminator and spectral discriminator. The conditional discriminator take the RGB image and generated or real HSI for input, and output an $N \times N$ metric for correspondence of the two inputs. Before the spectral discriminate, RGUS is used for sample spectra from HSI including steps patch divide and random sample. Then the selected spectra is input to the MLP based spectral discriminator.

B. Joint Discrimination: Conditional Discriminator

We design a joint discrimination for prompting the generator to produce more realistic spectra and ensure the correspondence between generated samples and input RGB. The joint discrimination is conducted by two discriminators, one is the conditional discriminator (*Con-D*) which with a input concatenating HSI and RGB images. For the *Con-D*, we adopt PatchGAN to avoid one value between 0 – 1 cannot express the whole generative result. With the input of RGB and HSI combined, the output of the *Con-D* is an $N \times N$ patch where each one corresponding to the conditional reality of a local area in the generated image. Different from the traditional GAN which the variable output evaluates the whole picture, our conditional *D* can consider the reality of each patch and integrate each one. Please see Table I for the detailed structure of conditional *D*.

C. Joint Discrimination: Spectral Discriminator

To improve the physical reality of the generated spectra, a spectral discriminator is provided. The main structure of the spectral discriminator (*Spe-D*) is an MLP with an input of one dim with 150 elements (a spectrum) and an output between 0-1 with details in Table II.

To comprehensively percept of the spectral curve shape information, MLP is adopt instead of 1D-CNN. The output is to select the first of the softmax layer which represents the probability of whether the spectrum is true.

TABLE I
STRUCTURE OF THE CONDITIONAL DISCRIMINATOR

Operation	Name	Size
-	Input	$153 \times 256 \times 256$
Conv 3x3		
Conv 3x3	Layer1	$256 \times 256 \times 256$
Leaky ReLU		
Conv 4x4, Stride=2		
Conv 3x3	Layer2	$512 \times 128 \times 128$
BatchNorm		
Leaky ReLU		
Conv 4x4, Stride=2		
Conv 3x3	Layer3	$1024 \times 64 \times 64$
BatchNorm		
Leaky ReLU		
Conv 4x4, Stride=2		
BatchNorm	Layer4	$1024 \times 32 \times 32$
Leaky ReLU		
Conv 4x4		
Output		$1 \times 31 \times 31$
Sigmoid		

TABLE II
STRUCTURE OF THE SPECTRAL DISCRIMINATOR

Operation	Name	Output Size
Linear(150,128)	Input	128
Linear(128,256)	Hidden-1	256
Linear(256,128)	Hidden-2	128
Linear(128,2)	Hidden-3	2
Softmax and select the first	Output	1

We extract a certain number of spectra from the HSI for spectral discriminator to improve the calculation efficiency and prevent over-fitting. To make the selected spectra more representative of the global spectral characteristics, we propose a Random Global Uniform Sampling (RGUS) technique. The RGUS can sample spectra evenly distributed in each position of the HSI, and with greater randomness. Details of RGUS is shown in Algorithm 1.

Algorithm 1 Random Global Uniform Sampling (RGUS)

Input: HSI data with size $N \times N$; Patch size for division $S \times S$;

Output: $M \times M$ spectra selected from the HSI;

- 1: Divide the input HSI into $M \times M$ patches with size $S \times S$, where $S \times M = N$;
- 2: Randomly generate two numbers a, b between 0 and S as the horizontal and vertical coordinates respectively;
- 3: Extract the spectra with the location $[a, b]$ in each patch and get $M \times M$ spectra;
- 4: **return** $M \times M$ spectra;

Force the output to 1 when training G to generate more real spectra and optimize them to 0 of the generated HSI (and the output of the real HSI to 1) to improve the discrimination performance of the spectral discriminator.

D. Loss Function

We use the L_1 loss and binary cross-entropy (BCE) loss to construct our loss functions. The goal of the generator is to generate pseudo-HSI to obey the real data distribution $p_{\text{data}}(x)$ as much as possible, which can fool the discriminator. For this purpose, we first constrain the proximity of each generated spectra with the real ones. L_1 loss is a pixel-wise loss and it can avoid the sensitivity to outliers and prone to over-smoothing of L_2 loss. Therefore, we choose L_1 loss in generator. Let y be the real HSI and x be the RGB image, z be the parameters in G , the output of G is $G(x, z)$, the L_1 loss can be calculated according to Equation (6).

$$\mathcal{L}_{L1} = \mathbb{E}_{x,y,z} [\|y - G(x, z)\|_1] \quad (6)$$

In addition, in order to fool the conditional discriminator, binary cross-entropy (BCE) is used for adversarial loss.

$$\begin{aligned} \mathcal{L}_{\text{conadv}}(G, D_{\text{con}}) &= \mathbb{E}_y [\log D_{\text{con}}(y)] \\ &+ \mathbb{E}_{x,z} [\log(1 - D_{\text{con}}(G(x, z)))] \end{aligned} \quad (7)$$

In the same way, the adverse loss of the spectral discriminator is

$$\begin{aligned} \mathcal{L}_{\text{speadv}}(G, D_{\text{spe}}) &= \mathbb{E}_y [\log D_{\text{spe}}(y)] \\ &+ \mathbb{E}_{x,z} [\log(1 - D_{\text{spe}}(G(x, z)))] . \end{aligned} \quad (8)$$

In summary, the loss of generator is in Equation (9), where λ_1 and λ_2 represent the weight coefficient between the three losses.

$$\mathcal{L}_G = \mathcal{L}_{L1} + \lambda_1 \mathcal{L}_{\text{conadv}}(G, D_{\text{con}}) + \lambda_2 \mathcal{L}_{\text{speadv}}(G, D_{\text{spe}}) \quad (9)$$

For discriminators, the optimization goal is to distinguish between generated HSI and the real, as Equation (10) and (11).

$$\begin{aligned} \max_{D_{\text{con}}} \mathcal{L}_{\text{conadv}}(G, D_{\text{con}}) &= \mathbb{E}_y [\log D_{\text{con}}(y)] \\ &+ \mathbb{E}_{x,z} [\log(1 - D_{\text{con}}(G(x, z)))] \end{aligned} \quad (10)$$

$$\begin{aligned} \max_{D_{\text{spe}}} \mathcal{L}_{\text{speadv}}(G, D_{\text{spe}}) &= \mathbb{E}_y [\log D_{\text{spe}}(y)] \\ &+ \mathbb{E}_{x,z} [\log(1 - D_{\text{spe}}(G(x, z)))] \end{aligned} \quad (11)$$

In total, the optimization process can be expressed as (12).

$$\begin{aligned} \mathcal{G}^* = \arg \min_G \max_{D_{\text{con}}, D_{\text{spe}}} & \mathcal{L}_{L1}(G) + \lambda_1 \mathcal{L}_{\text{conadv}}(G, D_{\text{con}}) \\ & + \lambda_2 \mathcal{L}_{\text{speadv}}(G, D_{\text{spe}}) \end{aligned} \quad (12)$$

E. Implementation

The training samples are a set of 256×256 image patches randomly cropped from RGB and corresponding HSI. During the spetral discrimination, we first select 4×4 spectra from the generated HSI and the spectra in the corresponding real HSI are also extracted. As for loss function, we set $\lambda_1 = \lambda_2 = 0.01$. For optimization, we adopt Adam Optimizer with $\beta_1 = 0.9, \beta_2 = 0.999$ and during the process, the two discriminators are trained together and take turn with G . Learning rate decreasing strategy is adopted, the initial learning rate of G , conditional D and spectral D are $1 \times e^{-4}$ and become 0.1 times the previous after every 300 epochs. In order to generate reliable results early, we firstly train 100 epochs of G to obtain preliminary results and then add the two discriminators into the training process to adjust the quality of generation. After two Ds join, every training G 3 iters, training the two Ds 1 iter.

IV. EXPERIMENT

In this section, we experiment with R2HGAN on GF5 dataset. We conduct a detailed introduction of the dataset and present different quantitative metrics on HSI construction. Then a comparison with other state-of-the-art generation methods is carried out. Finally, ablation studies of the architecture are stated.

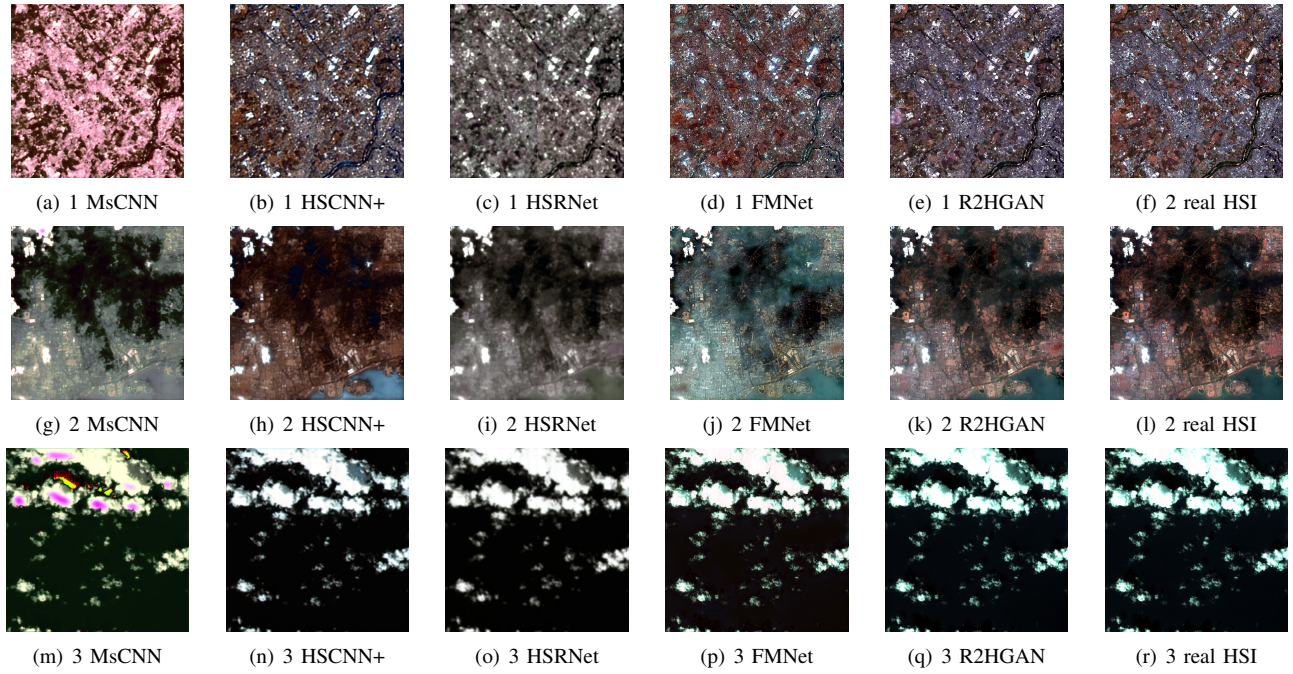


Fig. 2. False-color image of the generated HSI for three test images, (a), (b), (c), (d) and (e) show the result of MsCNN, HSCNN+, HSRNet, FMNet, R2HGAN respectively for image 1, the false-color of real HSI is in (f). (g), (h), (i), (j), (k) and (l) show the result and real HSI for image 2 and (m), (n), (o), (p), (q) and (r) show the result and real HSI for image 3.

A. Datasets and Experiment Setup

The dataset includes 6 scenes of hyperspectral including inland, island and sea. It covers cities, mountains, arable land, forests, ports, etc and the imaging time includes four seasons of 2018/2019. The HSIs are imaged by GF5 visible and near-infrared (VN) sensor with 16 bits (the range of reflection value is 0-65535). Each HSI has a total of 150 bands covering the wavelength range of $390nm - 1035nm$ with a nominal spectral resolution of 5 nm. The RGB images are extracted from the HSIs' bands 72, 35, 23. Each scene of the dataset has a spatial size of 2083×2008 and is cropped to 512×512 batches. Thus the dataset has 120 512×512 HSIs and corresponding RGB images. 115 image pairs are selected for training and 5 image pairs for testing.

The experiment is carried out under win10 system with Intel (R) Core (TM) i7-7700K CPU @ 4.20GHz and NVIDIA GeForce GTX 1080. The training process of R2HGAN takes approximately 19 hours. Under the same conditions, we compare R2HGAN to four spectral super resolution methods, including MsCNN [51], HSCNN+ [56], FMNet [84] and HSRNet [85]. MsCNN and HSCNN+ are based on U-Net and DenseNet respectively. FMNet adopts pixel-aware to keep pixel-learning ability. HSRNet uses physical mechanism, reconstructing according to Spectral Response Function (SRF).

To train all the deep-learning based methods adequately, we train them on the whole training set (115 image pairs) and chose different parameters by evaluate them on the testing set (5 image pairs). Therefore, we choose the parameters by selecting the best result of each method. All experiment settings are set same for R2HGAN and other four methods.

B. Comparison with Other Methods

We compare our R2HGAN with some state-of-the-art spectral super-resolution methods including MsCNN [51], HSCNN+ [56], FMNet [84] and HSRNet [85]. All these methods are fully optimized on our dataset under same condition to obtain the best performance for fair competition. The exception is that HSRNet is cropped during the test due to GPU memory limitations. Fig. 2 shows a comparison of the false-color images of the HSI generated by these methods. We can find that R2HGAN generates HSI whose false-color image closer to the real HSI. MsCNN has a large loss of both spatial and color information. HSCNN+ and HSRNet can maintain the spatial structure well, but lost information of the color. FMNet can better preserve color information while maintaining spatial structure relatively completely. R2HGAN has a good recovery of spatial and color information at the same time. The HSI generated by HSRNet has seams because of the limitation of GPU memory, we cut the RGB image input 512×512 into 256×256 and Re-splicing.

Table III shows the performance of different comparison methods on various indicators, including MPSNR, MRAE, RMSE to measure the result of image reconstruction, Spectral Angle Mapping (SAM) to quantity related to spectral shape and category information and MSSIM that measure the spatial structure. MPSNR represents RMSE and MRAE to a certain extent and $MAX_j = 65535$. From these indicators, we can find that FMNet is under-performing in terms of spatial structure, which is related to its use of pixel-aware. HSCNN+ and HSRNet perform relatively well on both spectral and spatial information except R2HGAN. R2HGAN performs better than any other comparing methods in five indicators. R2HGAN gets the highest MPSNR of 61.479 followed by HSRNet with

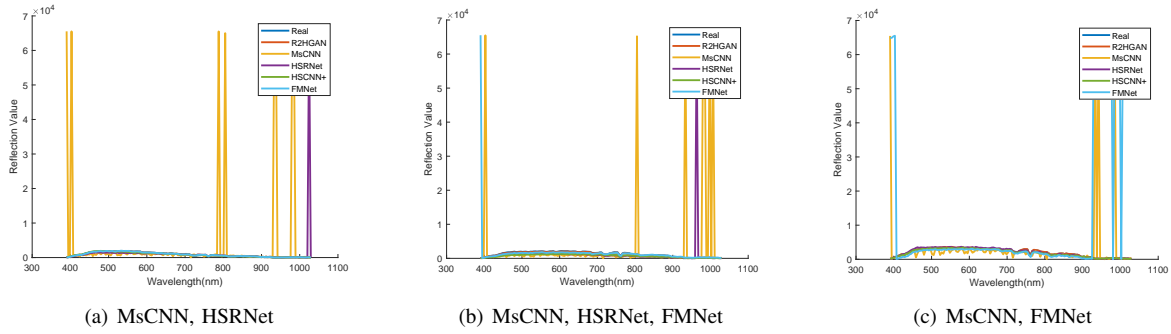


Fig. 3. Abnormal spectra generated by comparison methods. The title of the figure represents the methods generating abnormal spectra. In (a), MsCNN and HSRNet have abnormal generation. In (b), except for R2HGan and HSCNN+, other methods all generated abnormal spectra. In (c), MsCNN and FMNet have abnormal generation.

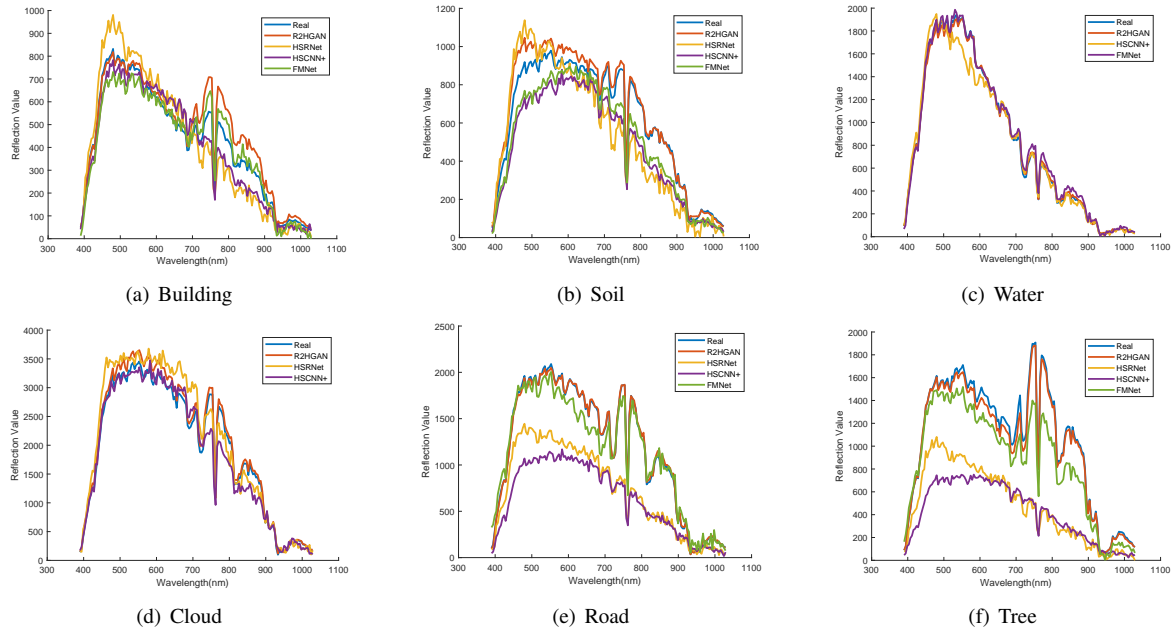


Fig. 4. Compare real spectra with those generated by various methods. (a-d) shows the spectra of different ground objects produced by five methods. The titles represent objects selected to plot spectra. R2HGAN generates spectra that are more like real ones on multi-objects.

48.166. Meanwhile, R2HGAN preserves the most structural information with $\text{MSSIM}=0.9972$ followed by HSCNN+. The SAM between R2HGAN generated HSIs and the real ones reaches as low as 0.0435, while HSCNN+ gets a second at 0.192 more than four times of R2HGAN.

TABLE III
A COMPARISON OF DIFFERENT METHODS ON OUR DATASET. FOR RMSE, MRAE, SAM AND RSRS A LOWER SCORE INDICATES BETTER, WHILE FOR MSSIM AND MPSNR A HIGHER SCORE INDICATES BETTER.

Method	RMSE ↓	MRAE ↓	SAM ↓	MSSIM ↑	MPSNR ↑
MsCNN [51]	23682	136.33	1.3539	0.7108	28.056
HSCNN+ [56]	2242	6.829	0.192	0.9432	46.273
HSRnet [84]	2625.2	5.997	0.4832	0.9426	48.166
FMNet [85]	7793.4	40.787	0.4842	0.8741	42.792
R2HGAN	178.3	0.126	0.0435	0.9972	61.479

Besides, our method can avoid generating abnormal or non-physical spectral curves. As shown in Fig. 3, the relatively competitive HSRNet and FMNet in the comparison method are both prone to outliers. Furthermore, MsCNN is almost

impossible to produce spectra without anomalies. R2HGAN has not been found to produce abnormal spectra.

We randomly select different objects and plot their spectra generated as well as the real ones. Fig. 4 shows the difference between spectra generated by five methods and the real ones. Please note that the lack of spectral curves from a certain method in some figures is due to the abnormal spectrum generated by the method. We only show the generated spectra which are similar to the real ones. It is obvious that R2HGAN generated spectra more like the real ones for various objects. Besides, FMNet performed relatively well, HSRNet and HSCNN+ performed poorly, and MsCNN was the worst, barely able to generate a normal spectrum.

In Fig. 5, some typical bands of the HSI generated by the five methods are exhibited. From left to right are respectively bands of MsCNN, HSCNN+, HSRNet, FMNet, R2HGAN, and the GroundTruth. The performance of MsCNN in all bands is far from the true value. Besides, all methods except MsCNN get a relatively close generation to the real HSI for band 60 in image 1. For band 10 and 80 in image 1, the five methods all

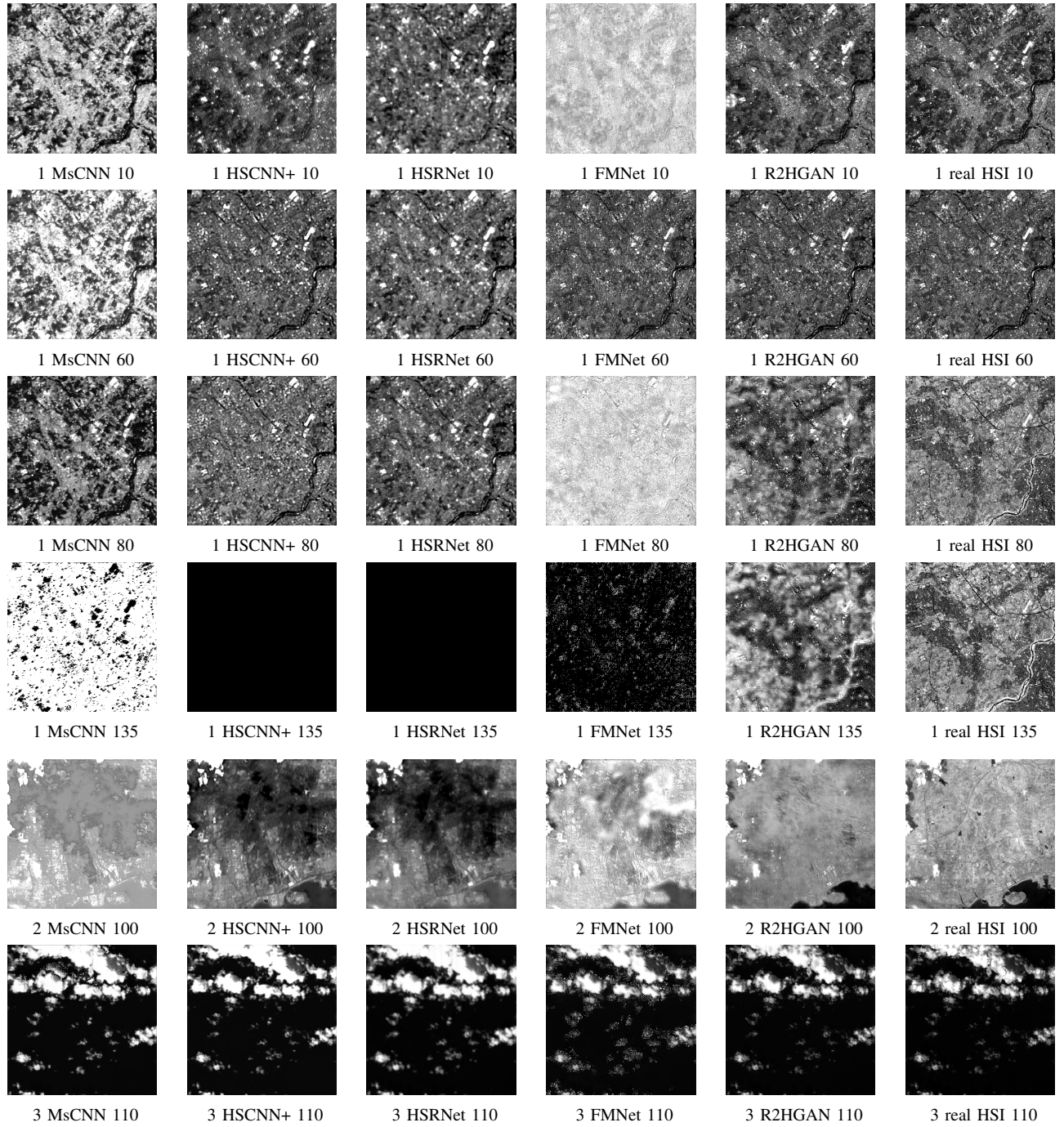


Fig. 5. Different bands of the generated HSI on three test images. Each row represents the effect of different methods on the same band, and each column represents the different bands of the same method to generate HSI. Numbers before the methods represent different test images and the following ones represent the index of the band. For example, 1 MsCNN 30 means it shows the 30th band in the HSI generated for image 1 by MsCNN.

distorted slightly in spatial details of the band and FMNet also caused brightness distortion. But for band 135 in image 1 and band 100 in image 2, all methods failed to generate reliable bands, only R2HGAN can reserve more spatial information. Test image 3 is relatively simple with cloud and sea water, but FMNet and MsCNN all cause abnormal points. Test image 3 is relatively simple with cloud and sea water, but FMNet and MsCNN all cause abnormal points.

C. Ablation Studies

The ablation studies are conducted to improve the effectiveness of the two discriminators. We compare the joint discrimination with conditional discriminator only or spectral discriminator only respectively.

1) Study of Joint Discrimination: Here we mainly analyze the excellence of joint discrimination. In Table IV, we demonstrate RMSE, MRAE, SAM, MSSIM, and MPSNR of 6 ablation experiments.

Comparing experiment 1 and 3 in Table IV, we can find the

TABLE IV

ABLATION STUDIES, THE CROSS IN BN MEANS MOVING BN FROM G, THE CHECK MARK MEANS WITH THE D OR RGUS. $Con\text{-}D$ REPRESENTS THE CONDITIONAL DISCRIMINATOR WHILE $Spe\text{-}D$ MEANS THE SPECTRAL ONE.

Name	BN	$Con\text{-}D$	$Spe\text{-}D$	RGUS	RMSE ↓	MRAE ↓	SAM ↓	MSSIM ↑	MPSNR ↑
1	X				1820.5	4.4045	0.1404	0.981	51.2877
2		✓	✓	✓	311.02	0.382	0.0742	0.991	58.1387
3	X	✓			357.62	0.37	0.0553	0.9952	59.4947
4	X		✓	✓	266.56	0.227	0.0477	0.9962	60.0801
5	X	✓	✓		204.91	0.162	0.0462	0.9965	60.7535
6	X	✓	✓	✓	143.23	0.1066	0.0418	0.9975	62.058

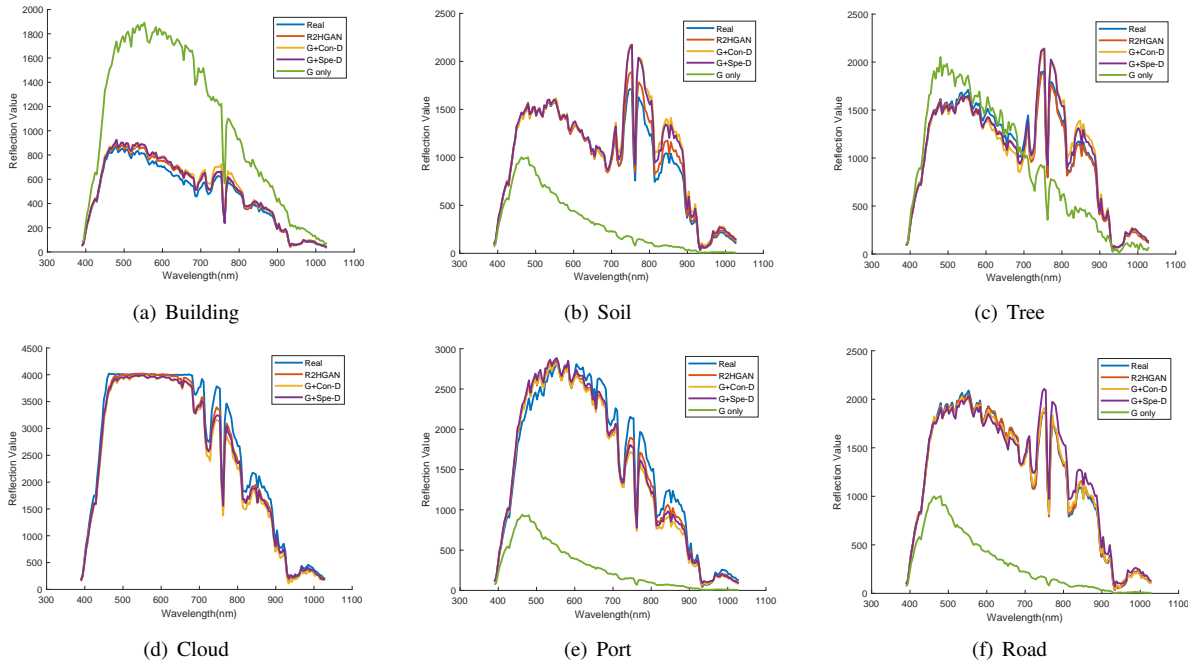


Fig. 6. Comparison of generated spectra after adding discriminators on different objects. R2HGAN represents the joint discrimination, $G+Con\text{-}D$ means only use conditional D and G only is the spectral without any discriminator.

introduce of the conditional discriminator greatly improved the generation effect that the MPSNR gains an increase of around 8.2. Meanwhile, the MSSIM also has a 1.4% improvement which means that the conditional discriminator enables the generator to recover more spatial structure information.

In experiment 4, only the spectral discriminator is adopted together with the RGUS. It can be seen that the addition of the spectral discriminator has greatly improved the quality of the generated spectra, and the PSNR has been increased from 51.29 to 60.08. At the same time, the spectral discriminator can obtain a lower SAM than the conditional discriminator.

The experiment 6 in Table IV shows the results of adopting joint discrimination and using RGUS sampling for spectral discriminator. And it is shown that with the discriminators, all indicators have improved. When we use conditional discriminator and spectral discriminator simultaneously, the spectra generated are more similar to the real ones that use G alone or G and conditional D . As is shown in Fig. 6, the G alone method causes a huge deviation in the generated spectra. R2HGAN represents the joint with the conditional and spectral discriminator, it generates spectra very close to the method with conditional D only. The spectral discriminator fine-tunes

the spectra to make it closer to real. For example, Fig. 6 (d) shows the spectra of a cloud pixel. The G only method generates spectrum far from the real. The conditional D and R2HGAN obtain spectra exactly alike, and the one from R2HGAN is more similar to the real.

2) *Ablation on RGUS*: For the spectral discriminator, we random select several spectra from the HSI. We design a Random Global Uniform Sampling (RGUS) technique to extract spectra which represent global spectral information of the HSI. For experiment 5 in Fig. IV, we random select the same number of spectra as RGUS for spectral discrimination. As compare between 5 and 6, the RGUS promotes the MPSNR from 60.75 to 61.30. Therefore, the global information by the RGUS is helpful for the generation.

Meanwhile, we compare the patch size of RGUS in Table V. A larger patch size results in fewer selected spectra, which reduces training time. Smaller patch size selects more spectra and causes consumption of the training time. As is shown in Table V, with the increase of patchsize in RGUS (M), the spectra input to $Spe\text{-}D$ reduce, the various indicators gradually improve till $M = 64$. Thus we select the patchsize as 64.

TABLE V
EXPERIMENT ON THE PATCH SIZE OF RGUS

Name	M in RGUS	RMSE ↓	MRAE ↓	SAM ↓	MSSIM ↑	MPSNR ↑
1	16	178.97	0.1189	0.0425	0.9973	60.939
2	32	178.28	0.1257	0.0435	0.9972	61.479
3	64	143.23	0.1066	0.0418	0.9975	62.058
4	128	162.32	0.1178	0.0417	0.9976	61.842

3) *Effect of removing BN in G:* From Table IV, experiment 2 and 6 show the different effects of whether to remove BN. Comparing with BN in G, the removal of it wons a 3.16 improvement of MPSNR as well as promoting of other indicators.

V. CONCLUSION

We propose a general framework for generating HSI from RGB images. The R2HGAN can generate reliable spectra while retaining more spatial information. We collect 6 scenes of HSI from GF5 for the experiment which different from the previous methods of conducting testing and training on one-scene HSI. And to overcome the ill-posedness during 3-150 bands generation and overfitting (over smooth), we design a joint discrimination method to distinguish the reality of the generation by discriminators two discriminators. The conditional discriminator based on PatchGAN measures the correspondence between the generated HSI and the input RGB. The spectral discriminator adopts MLP architecture to avoid the problem of CNN being affected by the receptive field. Furthermore, we newly design a random global uniform sampling (RGUS) method to extract spectra from the generated HSI for the spectral discriminator. The RGUS is closer to obtaining a subset of the global spectral expression. Ablation studies improve the effectiveness of our framework. Our method achieves better generation results than other state-of-the-art methods under the evaluation of multiple indicators. Codes of our R2HGAN are available on <http://levir.buaa.edu.cn/Code.htm>.

REFERENCES

- [1] P. Ghamisi, N. Yokoya, J. Li, W. Liao, S. Liu, J. Plaza, B. Rasti, and A. Plaza, "Advances in hyperspectral image and signal processing: A comprehensive overview of the state of the art," *IEEE Geoscience and Remote Sensing Magazine*, vol. 5, no. 4, pp. 37–78, 2017.
- [2] M. Borhani and H. Ghassemian, "Kernel multivariate spectral-spatial analysis of hyperspectral data," *IEEE Journal of Selected Topics in Applied Earth Observations and Remote Sensing*, vol. 8, no. 6, pp. 2418–2426, 2015.
- [3] N.-B. Chang, B. Vannah, and Y. Jeffrey Yang, "Comparative sensor fusion between hyperspectral and multispectral satellite sensors for monitoring microcystin distribution in lake erie," *IEEE Journal of Selected Topics in Applied Earth Observations and Remote Sensing*, vol. 7, no. 6, pp. 2426–2442, 2014.
- [4] B. Pan, Z. Shi, and X. Xu, "Mugnet: Deep learning for hyperspectral image classification using limited samples," *ISPRS Journal of Photogrammetry and Remote Sensing*, vol. 145, pp. 108 – 119, 2018, deep Learning RS Data.
- [5] L. Liu, Z. Shi, B. Pan, N. Zhang, H. Luo, and X. Lan, "Multi-scale deep spatial feature extraction using virtual rgb image for hyperspectral imagery classification," *Remote Sensing*, vol. 12, no. 2, p. 280, 2020.
- [6] D. Hong, L. Gao, J. Yao, B. Zhang, A. Plaza, and J. Chanussot, "Graph convolutional networks for hyperspectral image classification," *IEEE Transactions on Geoscience and Remote Sensing*, vol. 59, no. 7, pp. 5966–5978, 2021.
- [7] D. Hong, L. Gao, N. Yokoya, J. Yao, J. Chanussot, Q. Du, and B. Zhang, "More diverse means better: Multimodal deep learning meets remote-sensing imagery classification," *IEEE Transactions on Geoscience and Remote Sensing*, vol. 59, no. 5, pp. 4340–4354, 2021.
- [8] C.-I. Chang, "An effective evaluation tool for hyperspectral target detection: 3d receiver operating characteristic curve analysis," *IEEE Transactions on Geoscience and Remote Sensing*, pp. 1–23, 2020.
- [9] Z. Zou and Z. Shi, "Hierarchical suppression method for hyperspectral target detection," *IEEE Transactions on Geoscience and Remote Sensing*, vol. 54, no. 1, pp. 330–342, 2016.
- [10] T. Jiang, Y. Li, W. Xie, and Q. Du, "Discriminative reconstruction constrained generative adversarial network for hyperspectral anomaly detection," *IEEE Transactions on Geoscience and Remote Sensing*, vol. 58, no. 7, pp. 4666–4679, 2020.
- [11] Z. Shi, T. Shi, M. Zhou, and X. Xu, "Collaborative sparse hyperspectral unmixing using l_0 norm," *IEEE Transactions on Geoscience and Remote Sensing*, vol. 56, no. 9, pp. 5495–5508, 2018.
- [12] X. Xu, Z. Shi, and B. Pan, "L0-based sparse hyperspectral unmixing using spectral information and a multi-objectives formulation," *ISPRS journal of photogrammetry and remote sensing*, vol. 141, pp. 46–58, 2018.
- [13] D. Hong, N. Yokoya, J. Chanussot, and X. X. Zhu, "An augmented linear mixing model to address spectral variability for hyperspectral unmixing," *IEEE Transactions on Image Processing*, vol. 28, no. 4, pp. 1923–1938, 2019.
- [14] D. Hong, N. Yokoya, J. Chanussot, J. Xu, and X. X. Zhu, "Learning to propagate labels on graphs: An iterative multitask regression framework for semi-supervised hyperspectral dimensionality reduction," *ISPRS Journal of Photogrammetry and Remote Sensing*, vol. 158, pp. 35–49, 2019. [Online]. Available: <https://www.sciencedirect.com/science/article/pii/S0924271619302199>
- [15] K. Fotiadou, G. Tsagkatakis, and P. Tsakalides, "Spectral super resolution of hyperspectral images via coupled dictionary learning," *IEEE Transactions on Geoscience and Remote Sensing*, vol. 57, no. 5, pp. 2777–2797, 2019.
- [16] Z. Li, H. Shen, H. Li, G. Xia, P. Gamba, and L. Zhang, "Multi-feature combined cloud and cloud shadow detection in gaofen-1 wide field of view imagery," *Remote sensing of environment*, vol. 191, pp. 342–358, 2017.
- [17] D. P. Roy, M. A. Wulder, T. R. Loveland, C. E. Woodcock, R. G. Allen, M. C. Anderson, D. Helder, J. R. Irons, D. M. Johnson, R. Kennedy *et al.*, "Landsat-8: Science and product vision for terrestrial global change research," *Remote sensing of Environment*, vol. 145, pp. 154–172, 2014.
- [18] Y.-N. Liu, D.-X. Sun, X.-N. Hu, X. Ye, Y.-D. Li, S.-F. Liu, K.-Q. Cao, M.-Y. Chai, J. Zhang, Y. Zhang *et al.*, "The advanced hyperspectral imager: aboard china's gaofen-5 satellite," *IEEE Geoscience and Remote Sensing Magazine*, vol. 7, no. 4, pp. 23–32, 2019.
- [19] C. Yi, Y.-Q. Zhao, and J. C.-W. Chan, "Spectral super-resolution for multispectral image based on spectral improvement strategy and spatial preservation strategy," *IEEE Transactions on Geoscience and Remote Sensing*, vol. 57, no. 11, pp. 9010–9024, 2019.
- [20] T. Akgun, Y. Altunbasak, and R. Mersereau, "Super-resolution reconstruction of hyperspectral images," *IEEE Transactions on Image Processing*, vol. 14, no. 11, pp. 1860–1875, 2005.
- [21] H. Kwon and Y.-W. Tai, "Rgb-guided hyperspectral image up-sampling," in *2015 IEEE International Conference on Computer Vision (ICCV)*, 2015, pp. 307–315.
- [22] J. Hu, X. Jia, Y. Li, G. He, and M. Zhao, "Hyperspectral image

- super-resolution via intrafusion network,” *IEEE Transactions on Geoscience and Remote Sensing*, vol. 58, no. 10, pp. 7459–7471, 2020.
- [23] J. Li, R. Cui, B. Li, R. Song, Y. Li, Y. Dai, and Q. Du, “Hyperspectral image super-resolution by band attention through adversarial learning,” *IEEE Transactions on Geoscience and Remote Sensing*, vol. 58, no. 6, pp. 4304–4318, 2020.
- [24] K. Zheng, L. Gao, W. Liao, D. Hong, B. Zhang, X. Cui, and J. Chanussot, “Coupled convolutional neural network with adaptive response function learning for unsupervised hyperspectral super resolution,” *IEEE Transactions on Geoscience and Remote Sensing*, vol. 59, no. 3, pp. 2487–2502, 2021.
- [25] R. Dian, S. Li, L. Fang, T. Lu, and J. M. Bioucas-Dias, “Nonlocal sparse tensor factorization for semiblind hyperspectral and multispectral image fusion,” *IEEE Transactions on Cybernetics*, vol. 50, no. 10, pp. 4469–4480, 2020.
- [26] S. Mei, R. Jiang, X. Li, and Q. Du, “Spatial and spectral joint super-resolution using convolutional neural network,” *IEEE Transactions on Geoscience and Remote Sensing*, vol. 58, no. 7, pp. 4590–4603, 2020.
- [27] P. Arun, K. M. Buddhiraju, A. Porwal, and J. Chanussot, “Cnn based spectral super-resolution of remote sensing images,” *Signal Processing*, vol. 169, p. 107394, 2020.
- [28] B. J. Fubara, M. Sedky, and D. Dyke, “Rgb to spectral reconstruction via learned basis functions and weights,” in *2020 IEEE/CVF Conference on Computer Vision and Pattern Recognition Workshops (CVPRW)*, 2020, pp. 1984–1993.
- [29] S. Koundinya, H. Sharma, M. Sharma, A. Upadhyay, R. Manekar, R. Mukhopadhyay, A. Karmakar, and S. Chaudhury, “2d-3d cnn based architectures for spectral reconstruction from rgb images,” in *2018 IEEE/CVF Conference on Computer Vision and Pattern Recognition Workshops (CVPRW)*, 2018, pp. 957–9577.
- [30] U. B. Gewali, S. T. Monteiro, and E. Saber, “Spectral super-resolution with optimized bands,” *Remote Sensing*, vol. 11, no. 14, p. 1648, 2019.
- [31] P. Isola, J.-Y. Zhu, T. Zhou, and A. A. Efros, “Image-to-image translation with conditional adversarial networks,” in *Proceedings of the IEEE conference on computer vision and pattern recognition*, 2017, pp. 1125–1134.
- [32] J. Hu, Y. Li, and W. Xie, “Hyperspectral image super-resolution by spectral difference learning and spatial error correction,” *IEEE Geoscience and Remote Sensing Letters*, vol. 14, no. 10, pp. 1825–1829, 2017.
- [33] H. Irmak, G. B. Akar, and S. E. Yuksel, “A map-based approach for hyperspectral imagery super-resolution,” *IEEE Transactions on Image Processing*, vol. 27, no. 6, pp. 2942–2951, 2018.
- [34] X.-H. Han, B. Shi, and Y. Zheng, “Self-similarity constrained sparse representation for hyperspectral image super-resolution,” *IEEE Transactions on Image Processing*, vol. 27, no. 11, pp. 5625–5637, 2018.
- [35] Y. Xu, Z. Wu, J. Chanussot, and Z. Wei, “Nonlocal patch tensor sparse representation for hyperspectral image super-resolution,” *IEEE Transactions on Image Processing*, vol. 28, no. 6, pp. 3034–3047, 2019.
- [36] Y. Zhao, J. Yang, and J. C.-W. Chan, “Hyperspectral imagery super-resolution by spatspectral joint nonlocal similarity,” *IEEE Journal of Selected Topics in Applied Earth Observations and Remote Sensing*, vol. 7, no. 6, pp. 2671–2679, 2014.
- [37] S. Li, R. Dian, L. Fang, and J. M. Bioucas-Dias, “Fusing hyperspectral and multispectral images via coupled sparse tensor factorization,” *IEEE Transactions on Image Processing*, vol. 27, no. 8, pp. 4118–4130, 2018.
- [38] J. Xue, Y.-Q. Zhao, Y. Bu, W. Liao, J. C.-W. Chan, and W. Philips, “Spatial-spectral structured sparse low-rank representation for hyperspectral image super-resolution,” *IEEE Transactions on Image Processing*, vol. 30, pp. 3084–3097, 2021.
- [39] M. A. Veganzones, M. Simes, G. Licciardi, N. Yokoya, J. M. Bioucas-Dias, and J. Chanussot, “Hyperspectral super-resolution of locally low rank images from complementary multisource data,” *IEEE Transactions on Image Processing*, vol. 25, no. 1, pp. 274–288, 2016.
- [40] R. Dian, S. Li, and L. Fang, “Learning a low tensor-train rank representation for hyperspectral image super-resolution,” *IEEE Transactions on Neural Networks and Learning Systems*, vol. 30, no. 9, pp. 2672–2683, 2019.
- [41] Y. Fu, T. Zhang, Y. Zheng, D. Zhang, and H. Huang, “Hyperspectral image super-resolution with optimized rgb guidance,” in *2019 IEEE/CVF Conference on Computer Vision and Pattern Recognition (CVPR)*, 2019, pp. 11653–11662.
- [42] L. Zhang, J. Nie, W. Wei, Y. Li, and Y. Zhang, “Deep blind hyperspectral image super-resolution,” *IEEE Transactions on Neural Networks and Learning Systems*, pp. 1–13, 2020.
- [43] I. J. Goodfellow, J. Pouget-Abadie, M. Mirza, B. Xu, D. Warde-Farley, S. Ozair, A. Courville, and Y. Bengio, “Generative adversarial networks,” 2014.
- [44] R. A. Borsoi, T. Imbiriba, and J. C. M. Bermudez, “Super-resolution for hyperspectral and multispectral image fusion accounting for seasonal spectral variability,” *IEEE Transactions on Image Processing*, vol. 29, pp. 116–127, 2020.
- [45] S. Song, D. Gibson, S. Ahmadzadeh, H. O. Chu, B. Warden, R. Overend, F. Macfarlane, P. Murray, S. Marshall, M. Aitkenhead *et al.*, “Low-cost hyper-spectral imaging system using a linear variable bandpass filter for agritech applications,” *Applied optics*, vol. 59, no. 5, pp. A167–A175, 2020.
- [46] K. V. Mishra, M. Cho, A. Kruger, and W. Xu, “Spectral super-resolution with prior knowledge,” *IEEE Transactions on Signal Processing*, vol. 63, no. 20, pp. 5342–5357, 2015.
- [47] X. Sun, L. Zhang, H. Yang, T. Wu, Y. Cen, and Y. Guo, “Enhancement of spectral resolution for remotely sensed multispectral image,” *IEEE Journal of Selected Topics in Applied Earth Observations and Remote Sensing*, vol. 8, no. 5, pp. 2198–2211, 2015.
- [48] L. Yan, X. Wang, M. Zhao, M. Kaloorazi, J. Chen, and S. Rahardja, “Reconstruction of hyperspectral data from rgb images with prior category information,” *IEEE Transactions on Computational Imaging*, vol. 6, pp. 1070–1081, 2020.
- [49] B. Arad and O. Ben-Shahar, “Sparse recovery of hyperspectral signal from natural rgb images,” in *European Conference on Computer Vision*. Springer, 2016, pp. 19–34.
- [50] Y. Jia, Y. Zheng, L. Gu, A. Subpa-Asa, A. Lam, Y. Sato, and I. Sato, “From rgb to spectrum for natural scenes via manifold-based mapping,” in *2017 IEEE International Conference on Computer Vision (ICCV)*, 2017, pp. 4715–4723.
- [51] Y. Yan, L. Zhang, J. Li, W. Wei, and Y. Zhang, “Accurate spectral super-resolution from single rgb image using multi-scale cnn,” in *Chinese Conference on Pattern Recognition and Computer Vision (PRCV)*. Springer, 2018, pp. 206–217.
- [52] S. Galliani, C. Lanaras, D. Marmanis, E. Baltsavias, and K. Schindler, “Learned spectral super-resolution,” *arXiv preprint arXiv:1703.09470*, 2017.
- [53] J. Li, C. Wu, R. Song, W. Xie, C. Ge, B. Li, and Y. Li, “Hybrid 2-d3-d deep residual attentional network with structure tensor constraints for spectral super-resolution of rgb images,” *IEEE Transactions on Geoscience and Remote Sensing*, vol. 59, no. 3, pp. 2321–2335, 2021.
- [54] Y. Zhao, L.-M. Po, Q. Yan, W. Liu, and T. Lin, “Hierarchical regression network for spectral reconstruction from rgb images,” in *2020 IEEE/CVF Conference on Computer Vision and Pattern Recognition Workshops (CVPRW)*, 2020, pp. 1695–1704.
- [55] S. Nie, L. Gu, Y. Zheng, A. Lam, N. Ono, and I. Sato, “Deeply learned filter response functions for hyperspectral reconstruction,” in *2018 IEEE/CVF Conference on Computer Vision and Pattern Recognition*, 2018, pp. 4767–4776.
- [56] Z. Shi, C. Chen, Z. Xiong, D. Liu, and F. Wu, “Hscnn+: Advanced cnn-based hyperspectral recovery from rgb images,” in *2018 IEEE/CVF Conference on Computer Vision and Pattern*

- Recognition Workshops (CVPRW)*, 2018, pp. 1052–10528.
- [57] K. G. Lore, K. K. Reddy, M. Giering, and E. A. Bernal, “Generative adversarial networks for spectral super-resolution and bidirectional rgb-to-multispectral mapping,” in *2019 IEEE/CVF Conference on Computer Vision and Pattern Recognition Workshops (CVPRW)*, 2019, pp. 926–933.
- [58] A. Alvarez-Gila, J. Van De Weijer, and E. Garrote, “Adversarial networks for spatial context-aware spectral image reconstruction from rgb,” in *2017 IEEE International Conference on Computer Vision Workshops (ICCVW)*, 2017, pp. 480–490.
- [59] H. Peng, X. Chen, and J. Zhao, “Residual pixel attention network for spectral reconstruction from rgb images,” in *2020 IEEE/CVF Conference on Computer Vision and Pattern Recognition Workshops (CVPRW)*, 2020, pp. 2012–2020.
- [60] A. Odena, C. Olah, and J. Shlens, “Conditional image synthesis with auxiliary classifier gans,” in *International conference on machine learning*. PMLR, 2017, pp. 2642–2651.
- [61] T. Karras, S. Laine, and T. Aila, “A style-based generator architecture for generative adversarial networks,” in *Proceedings of the IEEE/CVF Conference on Computer Vision and Pattern Recognition*, 2019, pp. 4401–4410.
- [62] J.-Y. Zhu, T. Park, P. Isola, and A. A. Efros, “Unpaired image-to-image translation using cycle-consistent adversarial networks,” in *2017 IEEE International Conference on Computer Vision (ICCV)*, 2017, pp. 2242–2251.
- [63] A. Bulat, J. Yang, and G. Tzimiropoulos, “To learn image super-resolution, use a gan to learn how to do image degradation first,” in *Proceedings of the European conference on computer vision (ECCV)*, 2018, pp. 185–200.
- [64] S. Lei and Z. Shi, “Hybrid-scale self-similarity exploitation for remote sensing image super-resolution,” *IEEE Transactions on Geoscience and Remote Sensing*, 2021.
- [65] T. Salimans, I. Goodfellow, W. Zaremba, V. Cheung, A. Radford, and X. Chen, “Improved techniques for training gans,” in *NIPS’16 Proceedings of the 30th International Conference on Neural Information Processing Systems*, vol. 29, 2016, pp. 2234–2242.
- [66] S. Nowozin, B. Cseke, and R. Tomioka, “f-gan: training generative neural samplers using variational divergence minimization,” in *NIPS’16 Proceedings of the 30th International Conference on Neural Information Processing Systems*, vol. 29, 2016, pp. 271–279.
- [67] H. Zhang, T. Xu, H. Li, S. Zhang, X. Wang, X. Huang, and D. N. Metaxas, “Stackgan: Text to photo-realistic image synthesis with stacked generative adversarial networks,” in *Proceedings of the IEEE international conference on computer vision*, 2017, pp. 5907–5915.
- [68] E. Denton, S. Chintala, A. Szlam, and R. Fergus, “Deep generative image models using a laplacian pyramid of adversarial networks,” in *Proceedings of the 28th International Conference on Neural Information Processing Systems - Volume 1*, ser. NIPS’15. Cambridge, MA, USA: MIT Press, 2015, p. 14861494.
- [69] T. Karras, T. Aila, S. Laine, and J. Lehtinen, “Progressive growing of gans for improved quality, stability, and variation,” in *International Conference on Learning Representations*, 2018.
- [70] M. Mirza and S. Osindero, “Conditional generative adversarial nets,” *arXiv preprint arXiv:1411.1784*, 2014.
- [71] Z. Yi, H. Zhang, P. Tan, and M. Gong, “Dualgan: Unsupervised dual learning for image-to-image translation,” in *2017 IEEE International Conference on Computer Vision (ICCV)*, 2017, pp. 2868–2876.
- [72] T. Kim, M. Cha, H. Kim, J. K. Lee, and J. Kim, “Learning to discover cross-domain relations with generative adversarial networks,” in *ICML’17 Proceedings of the 34th International Conference on Machine Learning - Volume 70*, 2017, pp. 1857–1865.
- [73] J. Y. Zhu, R. Zhang, D. Pathak, T. Darrell, A. A. Efros, O. Wang, and E. Shechtman, “Toward multimodal image-to-image translation,” in *31st Annual Conference on Neural Information Processing Systems, NIPS 2017*, vol. 30, 2017, pp. 465–476.
- [74] X. Huang, M.-Y. Liu, S. J. Belongie, and J. Kautz, “Multimodal unsupervised image-to-image translation,” in *Proceedings of the European Conference on Computer Vision (ECCV)*, 2018, pp. 179–196.
- [75] T. Karras, S. Laine, M. Aittala, J. Hellsten, J. Lehtinen, and T. Aila, “Analyzing and improving the image quality of stylegan,” in *Proceedings of the IEEE/CVF Conference on Computer Vision and Pattern Recognition*, 2020, pp. 8110–8119.
- [76] S. Lei, Z. Shi, and Z. Zou, “Coupled adversarial training for remote sensing image super-resolution,” *IEEE Transactions on Geoscience and Remote Sensing*, vol. 58, no. 5, pp. 3633–3643, 2020.
- [77] J. Ma, W. Yu, C. Chen, P. Liang, X. Guo, and J. Jiang, “Pan-gan: An unsupervised pan-sharpening method for remote sensing image fusion,” *Information Fusion*, vol. 62, pp. 110–120, 2020.
- [78] W. Zhao, X. Chen, X. Ge, and J. Chen, “Using adversarial network for multiple change detection in bitemporal remote sensing imagery,” *IEEE Geoscience and Remote Sensing Letters*, pp. 1–5, 2020.
- [79] Z. Wu, J. Li, Y. Wang, Z. Hu, and M. Molinier, “Self-attentive generative adversarial network for cloud detection in high resolution remote sensing images,” *IEEE Geoscience and Remote Sensing Letters*, vol. 17, no. 10, pp. 1792–1796, 2020.
- [80] C. Shi, L. Fang, Z. Lv, and H. Shen, “Improved generative adversarial networks for vhr remote sensing image classification,” *IEEE Geoscience and Remote Sensing Letters*, pp. 1–5, 2020.
- [81] J. Feng, H. Yu, L. Wang, X. Cao, X. Zhang, and L. Jiao, “Classification of hyperspectral images based on multiclass spatiotemporal generative adversarial networks,” *IEEE Transactions on Geoscience and Remote Sensing*, vol. 57, no. 8, pp. 5329–5343, 2019.
- [82] A. Mehta, H. Sinha, P. Narang, and M. Mandal, “Hidegan: A hyperspectral-guided image dehazing gan,” in *2020 IEEE/CVF Conference on Computer Vision and Pattern Recognition Workshops (CVPRW)*, 2020, pp. 846–856.
- [83] Z. Wang, A. C. Bovik, H. R. Sheikh, and E. P. Simoncelli, “Image quality assessment: from error visibility to structural similarity,” *IEEE transactions on image processing*, vol. 13, no. 4, pp. 600–612, 2004.
- [84] L. Zhang, Z. Lang, P. Wang, W. Wei, S. Liao, L. Shao, and Y. Zhang, “Pixel-aware deep function-mixture network for spectral super-resolution,” in *Proceedings of the AAAI Conference on Artificial Intelligence*, vol. 34, no. 07, 2020, pp. 12 821–12 828.
- [85] J. He, J. Li, Q. Yuan, H. Shen, and L. Zhang, “Spectral response function-guided deep optimization-driven network for spectral super-resolution,” *IEEE Transactions on Neural Networks and Learning Systems*, 2021.



Liqin Liu received her B.S. degree from Beihang University, Beijing, China in 2018. She is currently working toward her doctorate degree in the Image Processing Center, School of Astronautics, Beihang University. Her research interests include hyperspectral image processing, machine learning and deep learning.



Sen Lei received his B.S. degree from the Image Processing Center, School of Astronautics, Beihang University in 2015. He is currently working toward his doctorate degree in the Image Processing Center, School of Astronautics, Beihang University. His research interests include deep learning and image super-resolution.



Zhenwei Shi (M'13) received his Ph.D. degree in mathematics from Dalian University of Technology, Dalian, China, in 2005. He was a Postdoctoral Researcher in the Department of Automation, Tsinghua University, Beijing, China, from 2005 to 2007. He was Visiting Scholar in the Department of Electrical Engineering and Computer Science, Northwestern University, U.S.A., from 2013 to 2014. He is currently a professor and the dean of the Image Processing Center, School of Astronautics, Beihang University. His current research interests include remote sensing image processing and analysis, computer vision, pattern recognition, and machine learning.

Dr. Shi serves as an Associate Editor for the *Infrared Physics and Technology*. He has authored or co-authored over 100 scientific papers in refereed journals and proceedings, including the IEEE Transactions on Pattern Analysis and Machine Intelligence, the IEEE Transactions on Neural Networks, the IEEE Transactions on Geoscience and Remote Sensing, the IEEE Geoscience and Remote Sensing Letters and the IEEE Conference on Computer Vision and Pattern Recognition. His personal website is <http://levir.buaa.edu.cn/>.

Ning Zhang received the Ph.D. degree in optical engineering from the Changchun Institute of Optics, Fine Mechanics and Physics, Chinese Academy of Sciences, Changchun, China, in 2012. He is currently a Senior Engineer with the Shanghai Aerospace Electronic Technology Institute, Shanghai, China. His current research interests include remote sensing image processing and electronic system design.

Xinzhong Zhu is currently a Research Fellow with the Shanghai Aerospace Electronic Technology Institute, Shanghai, China. His current research interests include high speed data processing and electronic system design.